



Reaction Sintering of $\text{Ca}_3\text{Co}_4\text{O}_9$ with BiCuSeO Nanosheets for High-Temperature Thermoelectric Composites

Richard Hinterding¹ · Desiree Rieks¹ · Patrick A. Kißling¹ · Lukas Steinbach¹ · Nadja C. Bigall¹ · Armin Feldhoff¹

Received: 20 September 2021 / Accepted: 8 November 2021 / Published online: 16 December 2021
© The Author(s) 2021

Abstract

Ceramic composites composed of oxide materials have been synthesized by reaction sintering of $\text{Ca}_3\text{Co}_4\text{O}_9$ with BiCuSeO nanosheets. *In situ* x-ray diffraction and thermogravimetric analyses of the compound powders were conducted to understand the phase transformations during heating up to 1173 K. Further thermogravimetric analyses investigated the thermal stability of the composites and the completion of reaction sintering. The microstructure of the formed phases after reaction sintering and the composition of the composites were investigated for varying mixtures. Depending on the amount of BiCuSeO used, the phases present and their composition differed, having a significant impact on the thermoelectric properties. The increase of the electrical conductivity at a simultaneously high Seebeck coefficient resulted in a large power factor of $5.4 \mu\text{W cm}^{-1} \text{K}^{-2}$, more than twice that of pristine $\text{Ca}_3\text{Co}_4\text{O}_9$.

Keywords Thermoelectrics · composites · $\text{Ca}_3\text{Co}_4\text{O}_9$ · BiCuSeO · oxides

Introduction

Thermoelectric Principles

Thermoelectricity is the conversion of thermal energy into electrical energy and vice versa. As one method of energy harvesting, the thermoelectric effect can help in the face of limited resources and a growing need for sustainable energy. To utilize thermoelectricity to a greater extent, further improvements regarding the power output and conversion efficiency of thermoelectric materials are necessary. The basic principles of thermoelectric energy conversion in a material are described by the transport equation in Eq. 1.^{1–3}

$$\begin{pmatrix} I_q \\ I_s \end{pmatrix} = \frac{A}{L} \begin{pmatrix} \sigma & \sigma \cdot \alpha \\ \sigma \cdot \alpha & \sigma \cdot \alpha^2 + \Lambda_{OC} \end{pmatrix} \cdot \begin{pmatrix} \Delta\varphi \\ \Delta T \end{pmatrix} \quad (1)$$

This integral form of the transport equation includes the coupling of the electrical charge I_q and entropy I_s currents of a material with a cross-sectional area A and a length L . A thermally induced electrical current emerges due to the electrical potential difference $\Delta\varphi$ and the temperature difference ΔT . The magnitude of the electrical current depends on three material parameters, viz. the electrical conductivity σ , the Seebeck coefficient α , and the electrically open-circuited entropy conductivity Λ_{OC} . All three parameters as well as their relationship with the heat conductivity λ_{OC} appear in Eq. 2, which defines the figure of merit $f^{3,4}$ or zT .^{3,5}

$$f = \frac{\sigma \cdot \alpha^2}{\Lambda_{OC}} = \frac{\sigma \cdot \alpha^2}{\lambda_{OC}} \cdot T := zT \quad (2)$$

The figure of merit of a thermoelectric material reflects the maximum energy conversion efficiency, while the power factor $PF = \sigma \cdot \alpha^2$ dominates the maximum electrical power output.⁶ Especially for high-temperature applications, where the provided heat is abundant, the power factor is at least equally important as the figure of merit.⁷

✉ Richard Hinterding
richard.hinterding@pci.uni-hannover.de

✉ Armin Feldhoff
armin.feldhoff@pci.uni-hannover.de

¹ Institute of Physical Chemistry and Electrochemistry,
Callinstr. 3A, 30167 Hannover, Germany

Thermoelectric Materials

Many different material classes compete with or complement each other in thermoelectrics. Tellurides,⁸ skutterudites,⁹ half-Heusler compounds,¹⁰ Zintl phases,¹¹ polymers¹² as well as oxides¹³ are among the most prominent ones. This work focuses on oxides and oxyselenides as components for thermoelectric composites. The greatest advantage of oxides in comparison with most other materials is their high thermal stability in air, which is important for actual applications.⁶ Within the class of *p*-type oxides, $\text{Ca}_3\text{Co}_4\text{O}_9$ (CCO) is nearly uncontested with respect to its thermoelectric performance. Its thermal stability up to 1220 K in air¹⁴ allows applications at high temperature, and its thermoelectric properties originate from the layered structure. Two incommensurate subsystems build up CCO, one consisting of CoO_2 and one of Ca_2CoO_3 . The CoO_2 unit with a misfit-layered CdI_2 structure type alternates with the Ca_2CoO_3 unit with a cutout rocksalt-type structure.¹⁵ The incommensurate structure results from the same *a* but distinct *b* parameters of the two subsystems being stacked along the shared *c*-axis.¹⁶ As a result of the layered structure, anisotropic transport properties with favorable thermoelectric characteristics within the *a*–*b*-plane emerge.^{17,18} BiCuSeO (BCSO) on the other hand is a layered oxyselenide with limited thermal stability up to 573 K in air.¹⁹ Its layered structure with alternating Bi_2O_2 and Cu_2Se_2 layers along the *c*-axis²⁰ also results in highly anisotropic transport properties.²¹ Moreover, the anisotropy is even more pronounced in nanosheets because of the quantum confinement effect,²² which can improve the thermoelectric properties substantially.²³ Despite its limited oxidation stability, the thermoelectric properties of BCSO result in a figure of merit above 1 when doped properly, mainly owing to a low thermal conductivity.²⁴ Due to the oxidation tendency of BCSO, the combination of CCO with BCSO at the high sintering temperature of CCO in air is expected to result in reaction sintering accompanied by phase transformations. These phase transformations may result in ceramic composites with enhanced thermoelectric properties. A selection of other reported materials for composite materials based on CCO are silver inclusions,^{25,26} silver with polymer,²⁷ Na_xCoO_2 ,²⁸ Na_xCoO_2 with $\text{Bi}_2\text{Ca}_2\text{Co}_2\text{O}_9$,²⁹ La_2NiO_4 ,³⁰ ZrO_2 ,³¹ Co_3O_4 ,³² or Fe with Ni particles³³ to name a few. Generally, the added heterointerfaces in composite systems can lead to a decreased mean free path of phonons and hence a reduced thermal conductivity,^{34,35} although this depends on the added phases. The performance outcome after reaction sintering is difficult to predict, and changes of the transport properties in the composites must be related to newly formed phases or altering compositions. Therefore, scanning electron microscopy

(SEM), x-ray diffraction (XRD) analysis, thermogravimetric analysis (TGA), transmission electron microscopy (TEM), and energy-dispersive x-ray spectroscopy (EDXS) were used in this work to understand the changes of the CCO-BCSO system during and after sintering.

Experimental Procedures

Chemicals

The chemicals used included calcium cobaltite ($\text{Ca}_3\text{Co}_4\text{O}_9$, CerPoTech, Norway), bismuth nitrate hydrate [$\text{Bi}(\text{NO}_3)_3 \cdot x \text{H}_2\text{O}$, Alfa Aesar, 99.999%], selenourea [$\text{SeC}(\text{NH}_2)_2$, Alfa Aesar, 99%], copper nitrate hemipentahydrate [$\text{Cu}(\text{NO}_3)_2 \cdot 2.5\text{H}_2\text{O}$, Aldrich Chemistry, $\geq 99.99\%$], potassium hydroxide (KOH, $\geq 85\%$), sodium hydroxide (NaOH, Carl Roth, $\geq 99\%$), and ethanol (Carl Roth, $\geq 99.8\%$).

Synthesis

CCO and BCSO powders were used to form the ceramic composites. Pristine CCO powder was purchased from CerPoTech (Tiller, Norway). Further processing of the CCO powder involved grinding in an agate mortar for 15 min and uniaxial pressing in a 16-mm die at 250 MPa and room temperature. The gained disks were sintered at 1173 K for 10 h with a heating rate of 2 K min^{-1} and cooling rate of 10 K min^{-1} under air. The sintered CCO was ground again and then ready to form composite mixtures. BCSO nanosheets were synthesized hydrothermally according to the instructions given by Samanta et al.³⁶ The declared amounts of chemicals were added to a large 200-ml Teflon-lined stainless-steel autoclave. To obtain the composites, washed BCSO and presintered CCO were mixed in an agate mortar at weight ratios of 5:95, 10:90, 20:80, and 30:70 for 15 min. The pressing and sintering processes were analogous to those described for pristine CCO.

Microstructure Analysis

Identification of phases and their purity was achieved by x-ray diffraction (XRD) analysis (Bruker AXS GmbH, Bruker D8 Advance) with Cu K_α radiation. *In situ* measurements were performed with an equipped heating chamber HTK1200N (Anton Paar). The heating and cooling rate as well as the total dwell time at 1173 K were programmed to be equal to the sintering conditions of the pressed disks. A synthetic air gas flow of 50 ml min^{-1} was applied. Differences occurred because of the use of noncompacted powder and additional dwell times at lower temperature due to the measurement duration. Powder diffraction files from the

ICDD database were used to evaluate the measured XRD patterns for the following compounds: $\text{Ca}_3\text{Co}_4\text{O}_9$ (Miyazaki et al.¹⁵ and PDF 00-058-0661), CoO (PDF 01-071-1178), Co_3O_4 (PDF 01-074-1657), CaCo_2O_4 (PDF 00-051-1760), BiCuSeO (PDF 01-076-6689), Bi_2SeO_2 (PDF 01-070-1549), Bi_2O_3 (PDF 01-075-4627), and $\text{Ca}_3\text{Co}_2\text{O}_6$ (PDF 01-089-2466). The four-dimensional superspace group $Cm(0\ 1 - p\ 0)$ (equivalent to $Bm(0\ 0\ \gamma)$) was used for CCO in accordance with literature^{15,37,38} to account for the incommensurate structure. Further analyses were carried out by electron microscopy. Cross-sections were prepared by embedding the samples in epoxy resin and applying a multistep polishing program completed by vibration polishing using a 50-nm Al_2O_3 suspension. Elemental maps were obtained by scanning electron microscopy (SEM, JEOL JSM-7610FPlus) at 15 kV with two energy-dispersive x-ray spectrometers (EDXS, XFlash 6/60). Further analyses of the powders were conducted using a different SEM (JEOL JSM-6700F) at 2 kV. Scanning transmission electron microscopy (STEM, JEOL JEM-2100F-UHR) equipped with EDXS (Oxford Instruments, INCA-200 TEM) was used to analyze the main phase CCO. High-resolution TEM (HRTEM) and selected-area electron diffraction (SAED) were carried out at 200 kV. Thermogravimetric characteristics were measured with a TGA/DSC3+ from Mettler Toledo at a heating rate of $2\ \text{K}\ \text{min}^{-1}$ and air flow of $20\ \text{ml}\ \text{min}^{-1}$. The density of the sintered disks was determined by using the Archimedes method (ISO 5018:1983) with isopropanol as fluid.

Thermoelectric Analysis

The electrical conductivity and Seebeck coefficient were measured perpendicular to the pressing direction by cutting the sintered disks into bars with length of 10 mm and width of 3 mm. The electrical conductivity was measured by the four-point probe method at equilibrium conditions within a horizontal three-heating-zone tube furnace (Carbolite Gero EVZ 12/450B). The Seebeck coefficient was determined by using a ProboStat A setup from NorECs with a vertical furnace from Elite Thermal Systems Ltd. at equilibrium conditions. Values were recorded after heating to the maximum temperature of 1073 K and cooling in steps of 100 K to room temperature with intermediate dwell times to maintain stable conditions. The measurement setup included Keithley multimeters and LabVIEW data processing software.

Results and Discussion

CCO and BCSO powders were mixed to obtain the ceramic composites. The CCO was presintered and then ground to achieve higher crystallinity (compare the XRD and SEM measurements in Supplementary Fig. S1) and increased

density (Fig. S2) in the sintered ceramics with positive effects on the electrical conductivity. Only presintered CCO powder was used for the composites. BCSO was synthesized hydrothermally with minor Bi_2SeO_2 impurities, as proven by the XRD results in Supplementary Fig. S1a. The crystal habitus of BCSO was examined by SEM, and nanosheets with thickness of approximately 50 nm and lateral extension of up to 1000 nm were observed (cf. Supplementary Fig. S1b).

As BCSO is not stable at high temperature in air, changes in the composition of the sintered CCO-BCSO composites were expected. Beginning with the EDXS analysis, the elemental overlay maps in Fig. 1 provide more information on the resulting phases. The first difference between the CCO and the sample with 10 wt% BCSO is the crystal growth of CCO to large plate-like particles with lateral size of roughly $10\ \mu\text{m}$. This effect became even more pronounced with increasing BCSO amount and is likely caused by extensive restructuring of the CCO. Furthermore, a secondary cobalt oxide phase arises with particle size of approximately $1\ \mu\text{m}$

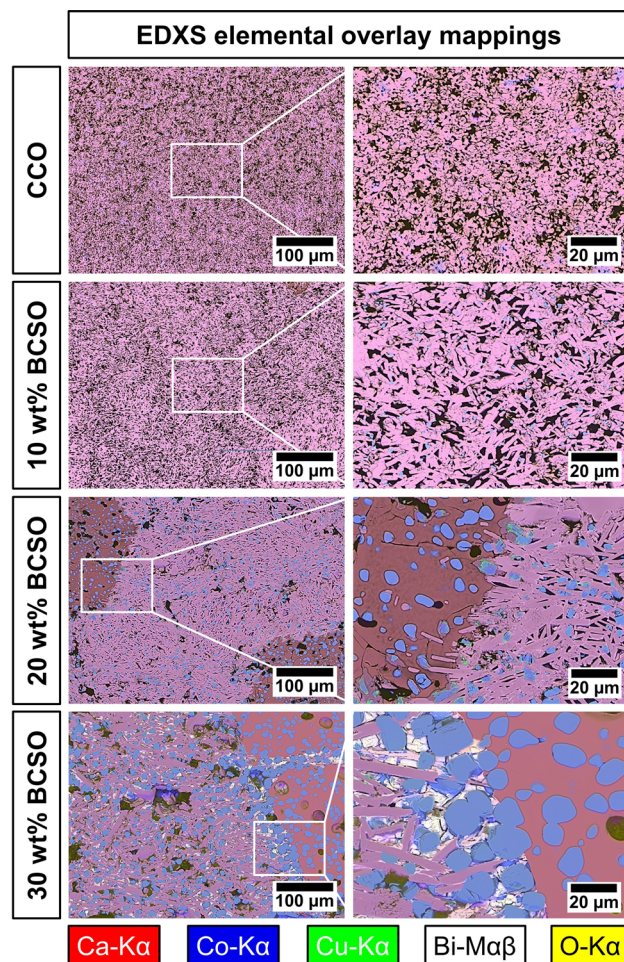


Fig. 1 Cross-sectional EDXS elemental overlay maps of CCO and composites with 10 wt.%, 20 wt.%, and 30 wt.% BCSO. See Supplementary Figs. S3–S10 for more details.

for the sample with 10 wt.% BCSO. These cobalt oxide particles grew to size of up to $20\ \mu\text{m}$ when the amount of BCSO was increased to 20 wt.% and 30 wt.%. A third phase of $\text{Ca}_3\text{Co}_2\text{O}_6$ emerged at 20 wt.% BCSO, which also incorporated cobalt oxide particles but did not show distinct crystal grains, which could indicate amorphous structure. Finally, a fourth phase of Bi_2O_3 became obvious for the 30 wt.% sample, being located between the CCO grains. The phases were identified by evaluating the quantitative EDXS results in Fig. 2, based on the average value of five particles for each phase and mapping. All the cross-sectional EDXS mappings performed at various magnifications are shown in Supplementary Fig. S3–S10. Note that no Se was detected in any of the composites, indicating evaporation or sublimation of a Se species during sintering.

The elemental composition of the CCO shows where Bi from the original BCSO remains. However, a doping limit seems to be reached at 20 wt.% BCSO as the amount of Bi does not increase further for the 30 wt.% sample. This explains the occurrence of the $\text{Bi}_2\text{O}_3\text{:Co,Ca}$ phase only for high amounts of BCSO because excess Bi cannot be incorporated into the CCO anymore. The substitution of Co with Bi in CCO leads to formation of $\text{Co}_3\text{O}_4/\text{CoO}\text{:Cu,Ca}$. Co_3O_4 and cubic CoO are both thermodynamically stable cobalt oxides in air at room temperature^{39,40} and cannot easily be distinguished by EDXS. Both phases can transfer reversibly into each other depending on the oxidation or reduction conditions.⁴⁰ At temperatures above 513 K in air, cubic CoO usually transforms rapidly into Co_3O_4 ³⁹. As the composites were sintered for several hours at this temperature in air, one can assume that only Co_3O_4 will be left. As the sintering temperature of 1173 K is slightly above the decomposition temperature of 1170 K for Co_3O_4 into CoO,⁴¹ both oxides can be expected in the sintered ceramic. This is proven by the XRD patterns of the 20 wt.% and 30 wt.% BCSO samples shown in Supplementary Fig. S11, which clearly show

the presence of CoO as well as Co_3O_4 within the composites. Furthermore, the amount of Cu in the cobalt oxides clearly increased with the amount of BCSO introduced. As only Cu but no Bi was found in the cobalt oxides, initial formation of CoO can be concluded based on the oxidation states of the metals, followed by partial oxidation to Co_3O_4 . $\text{Ca}_3\text{Co}_2\text{O}_6$ is a typical decomposition product of CCO,¹⁴ and its composition does not alter with increasing amounts of BCSO. Such decomposition could be caused by exothermic reactions during sintering, locally increasing the temperature above the decomposition temperature of CCO when agglomerates of BCSO are present. This is reasonable since the sintering temperature of 1173 K is close to the decomposition temperature of 1220 K.¹⁴ Another explanation is oxidation and decomposition of BCSO during sintering. The oxygen required for the formation of oxides could be derived from CCO, facilitating decomposition of CCO. This is especially the case when atmospheric oxygen cannot move freely within the compacted disk during sintering. As cobalt oxides are also decomposition products of CCO, this further explains the growth of these particles for the samples with 20 wt.% and 30 wt.% BCSO.

To understand the process during reaction sintering, *in situ* XRD analysis of the powder with 20 wt.% BCSO and 80 wt.% CCO was performed in air. The results (Fig. 3) show the progression of the phases formed during the whole sintering process. Noteworthy changes in reflections are highlighted, and the CCO and BCSO reflections are indexed at the starting temperature of 303 K. As expected, the BCSO decomposes at 573 K, which becomes obvious when looking at the vanishing 102 and 200 reflections. With the decomposition of BCSO, formation of Bi_2O_3 begins, and at 773 K, this phase even shows the most intense reflection of the composite (see $2\theta = 27.5^\circ$). At 873 K, the bismuth oxide also decomposes until it completely disappears at 1073 K. Another intermediate phase is CuO, which becomes

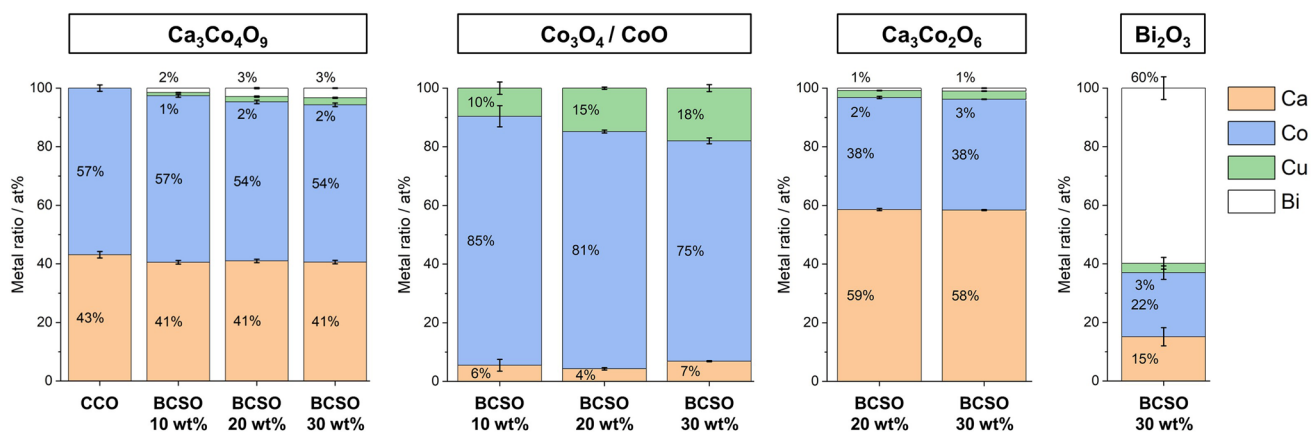


Fig. 2 EDXS-based quantification of compounds occurring in pristine CCO and composites with 10 wt.%, 20 wt.%, and 30 wt.% BCSO. Values are averages from five different spots within the elemental mappings of Fig. 1.

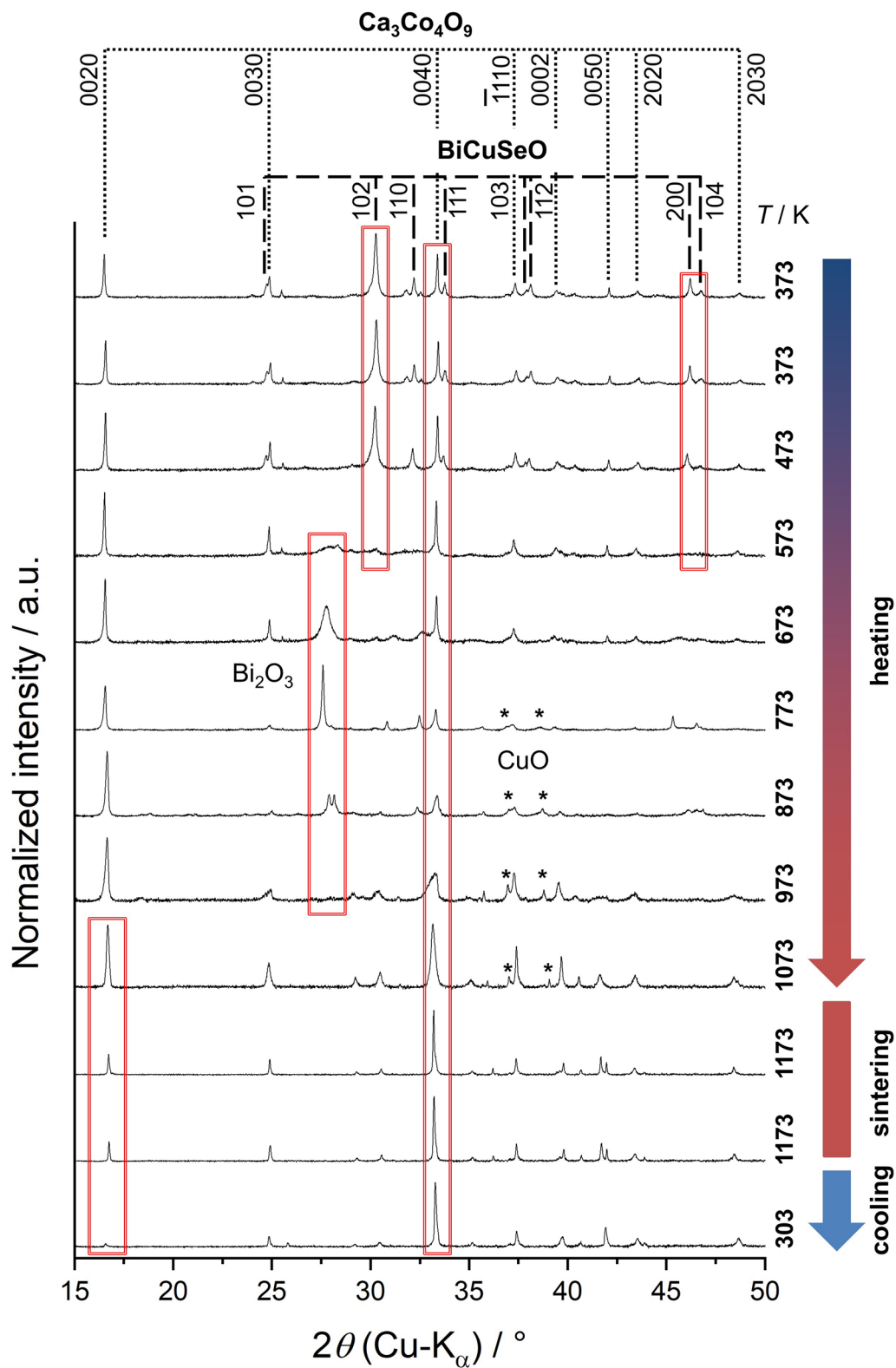


Fig. 3 *In situ* powder XRD monitoring of reaction sintering of the sample containing 20 wt.% BCSO and 80 wt.% CCO. From top to bottom, the temperature increases from room temperature to the maximum

temperature of 1173 K in steps of 100 K followed by cooling. Starting materials CCO and BCSO are indexed, and domains with noteworthy alteration are highlighted.

distinct at 773 K but vanishes at the maximum temperature of 1173 K. No crystalline selenium phases apart from BCSO at the beginning could be detected at any temperature step. The diffraction pattern when first reaching 1173 K is almost identical to that after the full sintering duration of 10 h, indicating that the phase transformations were completed. In the final product after sintering and cooling to 303 K, mainly reflections of CCO remain, but the intensity ratio is shifted in comparison with sintered CCO disks (cf. Supplementary Fig. S11). The main reason for this is the random orientation of the powder in comparison with the preferred orientation after uniaxial pressing. It is also related to the growth process of CCO to large plate-like CCO particles as depicted in the EDXS mappings. The 0040 reflection of CCO first diminishes compared with the 0020 reflection

until a temperature of 773 K is reached. At 873 K, the 0040 reflection intensifies and becomes the most intense during sintering. This indicates massive rearrangement within the CCO during the heating process and is related to the integration of Bi and Cu into the CCO structure. Generally, a strong preferred orientation or even texture is beneficial for CCO, because of its better thermoelectric properties along the a - b -plane.^{17,18}

Further information about the phases present during and after sintering was acquired by thermogravimetric analyses (Fig. 4a, b). The mass gain at 573 K can be attributed to the decomposition temperature of BCSO¹⁹ as confirmed by *in situ* XRD analysis and suggests the formation of oxides. The maximum mass occurs at 773 K, where Bi_2O_3 is the dominant crystalline phase according to the *in situ* XRD

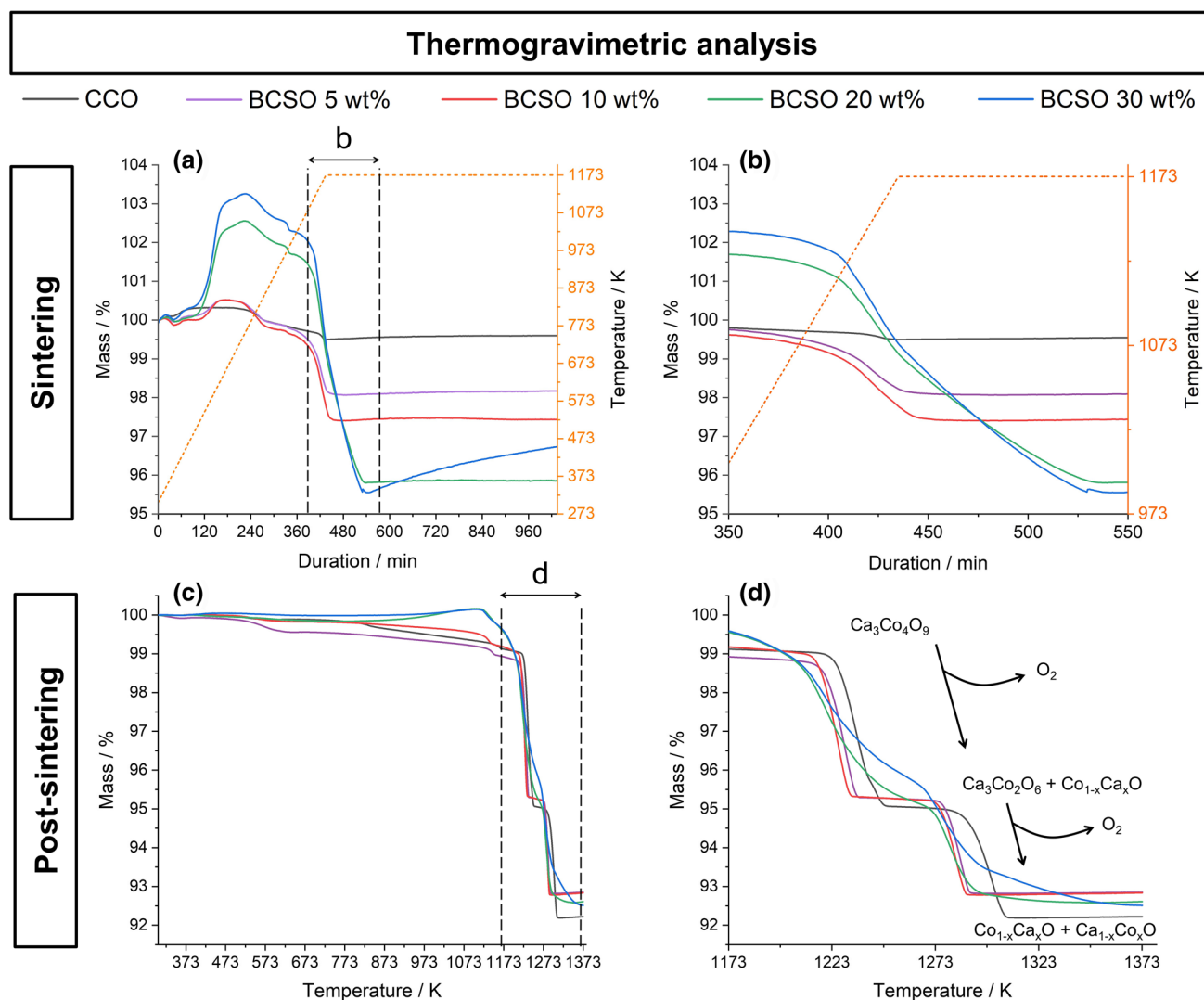


Fig. 4 Thermogravimetric analyses of unsintered powders and sintered ceramics of pristine CCO and composites. (a, b) Mass change and temperature against the duration of the applied sintering method

for the compound powders. (c, d) Mass change against the temperature for the sintered ceramics.

analysis. The decomposition of Bi_2O_3 between 873 K and 973 K is accompanied by a mass loss of approximately 1 wt.%. This mass loss is likely related to the incorporation of Bi into the CCO structure under release of oxygen. The most intense mass loss occurs between 973 K and 1173 K, being due to evaporation or sublimation of the Se species. As confirmed by the elemental mappings before, no Se was present in the sintered ceramics. Therefore, the loss of 4 wt.% for the sample with 20 wt.% BCSO in Fig. 4b must be attributed to a Se species with Cu and Bi still present within the composites. Furthermore, CCO shows only a small loss of less than 0.5 wt.% in this region, which is an expected phenomenon and linked to the variable and temperature-dependent amount of oxygen within the structure.⁴² For the samples with 5 wt.% to 20 wt.% BCSO, a plateau is reached at the sintering temperature of 1173 K, indicating that the reactions were completed and a stable composite resulted. However, the sample with 30 wt.% BCSO showed steady mass gain during the dwell time, indicating that oxygen was incorporated. As Bi_2O_3 is only found in significant amounts in this sample after sintering, the mass gain is likely caused by its formation. To prove the stability and decomposition temperature of the sintered composites, further thermogravimetric investigations were performed (Fig. 4c, d). Until 1173 K, only a small loss of up to 1 wt.% occurs for all the composites and the CCO, which can be attributed to oxygen reordering in CCO. The decomposition of CCO occurs at roughly 1223 K, in good agreement with literature data.¹⁴ For the composites, the decomposition temperature range widens due to the structural changes of CCO by incorporating Bi and Cu. Another mass loss is located at 1298 K, where $\text{Ca}_3\text{Co}_2\text{O}_6$ fully decomposes into calcium oxide and cobalt oxide, in agreement with literature¹⁴. The presence of both steps in all the composites supports the assumption that CCO is still the main phase.

The CCO within the sample with 20 wt.% BCSO was further investigated by TEM to verify its crystallinity after the growth to large plate-like particles. As shown in Fig. 5, the CCO showed high crystallinity as confirmed by the SAED results in Fig. 5b. No other phases or different orientations were observed for the investigated grain along the [0100] zone axis. The pairwise occurrence of reflections close to each other can be explained by microtwins, which have been observed for CCO previously.³⁰ The high-resolution TEM results in Fig. 5c, d clearly show the stacking order along the *c*-axis, while the bright lines are associated with the CoO_2 layers.⁴³ The dimension of the *c*-axis at 11.00 Å is slightly larger in comparison with the value of 10.84 Å for pure CCO,¹⁵ which can be attributed to the incorporation of Bi into the structure. The ionic radius of Bi^{3+} of 103 pm is clearly larger than the value of 0.55 pm for Co^{3+} , thus the expansion of the unit cell to some extent seems reasonable and further confirms the doping of CCO.

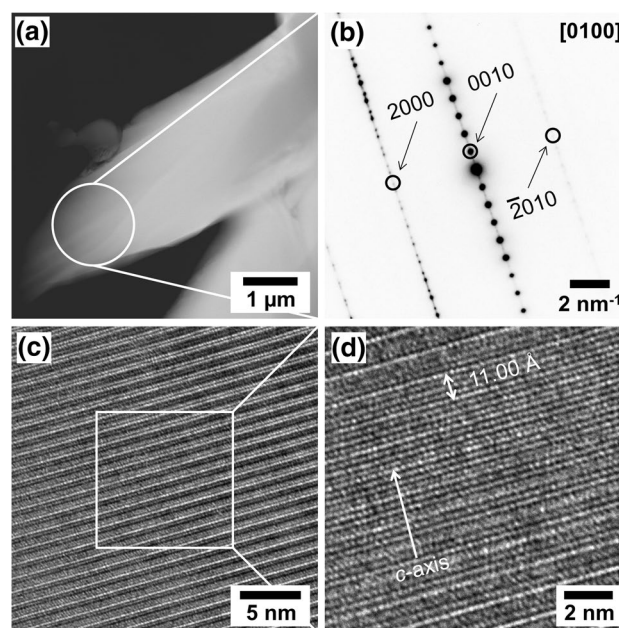


Fig. 5 Cross-sectional TEM characterization of the 20 wt.% BCSO sample. (a) STEM annular dark-field micrograph showing cross-section of a CCO sheet and the investigated area for SAED. (b) SAED pattern of CCO along the [0100] zone axis. Reflections were indexed by the four-dimensional superspace group approach.¹⁵ (c, d) High-resolution TEM showing the stacking order along the crystallographic *c*-axis and its dimension.

Based on the results of the analyses described so far, the outcome of reaction sintering of CCO and BCSO at different weight ratios is presented in Fig. 6. During the sintering process, the BCSO oxidizes and the Se species leaves the composite. While the CCO restructures and grows, Bi and Cu are incorporated and doped CCO results. The substituted Co and Ca form doped cobalt oxides with atmospheric oxygen. Further reactions occur for the same with 20 wt.% BCSO, where the CCO decomposition product $\text{Ca}_3\text{Co}_2\text{O}_6\text{:Bi,Cu}$ appears. Finally, $\text{Bi}_2\text{O}_3\text{:Co,Ca}$ emerges at 30 wt.% BCSO as the solubility limits of Bi are reached within the CCO.

Finally, the thermoelectric properties in terms of the electrical conductivity and Seebeck coefficient were measured and are shown in Fig. 7. The electrical conductivity in Fig. 7a increases with the amount of BCSO until reaching a maximum of 144 S cm^{-1} at 20 wt.% and 1073 K. The substantial decrease observed for the 30 wt.% sample is likely caused by the more dominant Bi_2O_3 phase, which even at high temperature has a relatively low electrical conductivity below 1 S cm^{-1} .⁴⁴ However, small amounts of Bi_2O_3 between CCO grains have proven to be beneficial to the thermoelectric properties by decreasing the grain-boundary resistivity.⁴⁵ The noticeable increase in density for the 20 wt.% BCSO sample (Supplementary Fig. S2) could also be linked to the Bi_2O_3 formation during the sintering process caused by liquification during sintering

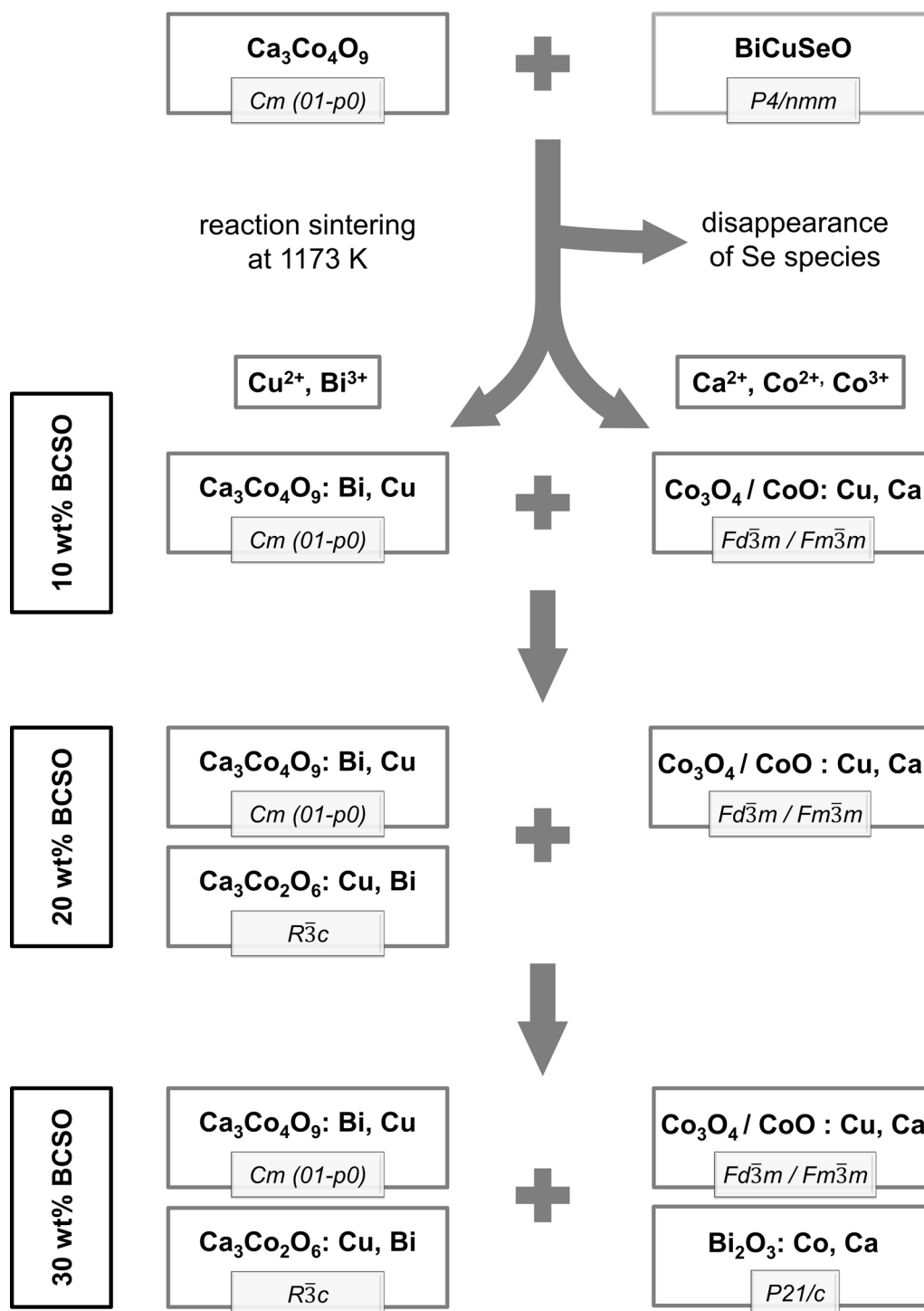


Fig. 6 Schematic of reaction sintering between CCO and BCSO. Depending on the amount of BCSO added, different phases emerge.

and reducing the sintering temperature.⁴⁶ Furthermore, the temperature dependence of the electrical conductivity increases with the amount of BCSO, which is also reflected in the Arrhenius plot in Supplementary Fig. S12 and the corresponding rise of the activation energies. The general progression of the Seebeck coefficient with

temperature is similar for all the investigated composites, but increased values can be noted despite the increasing electrical conductivity. This can be explained by the doping of CCO with Bi and Cu, which independently from each other have been proven to enhance the Seebeck coefficient and even the electrical conductivity.^{45,47} The

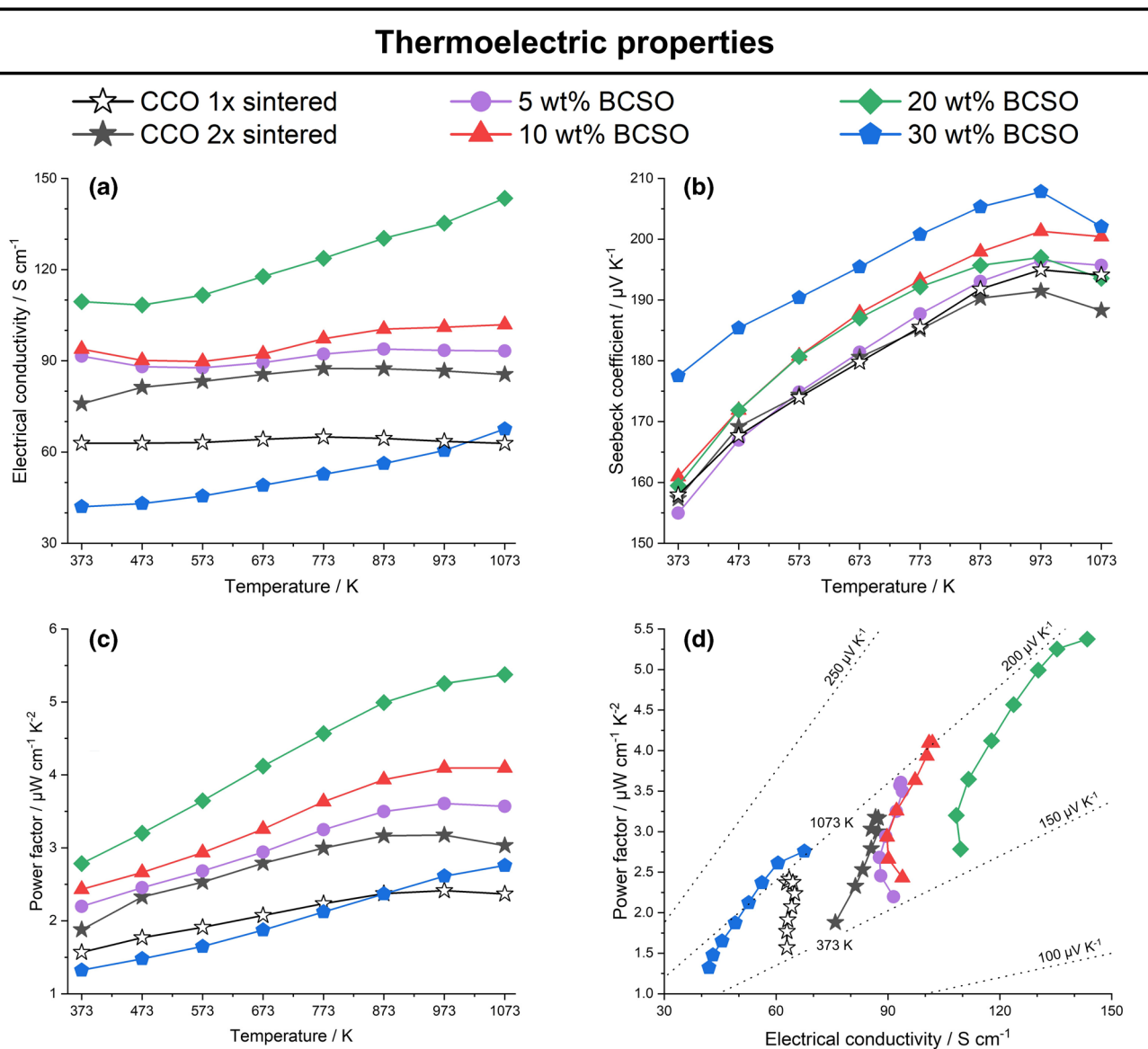


Fig. 7 Thermoelectric properties of sintered CCO and respective composites with 5 wt.%, 10 wt.%, 20 wt.%, and 30 wt% BCSO. (a) Electrical conductivity with maximum value for 20 wt.% BCSO at 1073 K. (b) Seebeck coefficient with higher values for all investigated

resulting power factor in Fig. 7c shows an improved value of $5.4\ \mu\text{W cm}^{-1}\text{ K}^{-2}$ for 20 wt.% BCSO in comparison with $2.9\ \mu\text{W cm}^{-1}\text{ K}^{-2}$ for double-sintered CCO and $2.37\ \mu\text{W cm}^{-1}\text{ K}^{-2}$ at 1073 K. Hence, the power factor is more than doubled. This becomes more obvious in the type I Ioffe plot in Fig. 7d. The plot of the power factor against the electrical conductivity summarizes the previous diagrams in Fig. 7a–c in one diagram. The improved power factor can clearly be attributed to the increase of the electrical conductivity as the Seebeck coefficient does not alter significantly. As stated by Narducci⁷, the power factor is an equally important value as the figure of merit zT for

composites in comparison with pristine CCO. (c) Power factor with maximum values for the 20 wt.% BCSO sample. (d) Type I Ioffe plot showing the power factor against electrical conductivity, condensing the results of a–c into one clear graph.

limitless energy sources, which are more likely to have high temperature⁶.

Conclusions

$\text{Ca}_3\text{Co}_4\text{O}_9$ and BiCuSeO were combined for the first time to create composites after reaction sintering. Presintering of $\text{Ca}_3\text{Co}_4\text{O}_9$ before use as a component enabled a higher density and increased electrical conductivity. As expected, the BCSO did not withstand the high sintering temperature of 1173 K in air, but the resulting reactions enabled *in situ*

doping of Ca₃Co₄O₉ with Bi and Cu as well as the formation of other doped oxide phases. XRD, SEM, EDXS, TGA, and TEM analyses revealed the phases in the final ceramic composites and possible intermediates during sintering. The high-temperature stability of the sintered ceramics was confirmed by TGA. Overall, the composites with up to 20 wt.% BiCuSeO were superior to pristine Ca₃Co₄O₉ in terms of the thermoelectric power factor. Formation of unfavorable Bi₂O₃ was observed at a share of 30 wt.% due to the solubility limits in Ca₃Co₄O₉. The best power factor of 5.4 μW cm⁻¹ K⁻² was achieved for the 20 wt.% BiCuSeO sample at 1073 K because of a substantial increase of the electrical conductivity while maintaining a high Seebeck coefficient. This resulted in a value more than twice as high as that of pristine Ca₃Co₄O₉ and shows the great potential of these composite systems based on more subtle adjustment of the weight ratio in the future.

Supplementary Information The online version contains supplementary material available at <https://doi.org/10.1007/s11664-021-09336-2>.

Acknowledgments The authors gratefully appreciate access to the JSM-6700FPlus by Dr. Renat Almeev and technical assistance by Frank Steinbach. The study was partly funded by Deutsche Forschungsgemeinschaft (DFG, German Research Foundation) projects FE 928/21-1 and BI 1708/5-1.⁴⁸ In addition, the project leading to these results has in part received funding from the European Research Council (ERC) under the European Union's Horizon 2020 research and innovation program (grant agreement no. 714429).

Funding Open Access funding enabled and organized by Projekt DEAL.

Conflict of interest The authors declare that they have no conflicts of interest.

Open Access This article is licensed under a Creative Commons Attribution 4.0 International License, which permits use, sharing, adaptation, distribution and reproduction in any medium or format, as long as you give appropriate credit to the original author(s) and the source, provide a link to the Creative Commons licence, and indicate if changes were made. The images or other third party material in this article are included in the article's Creative Commons licence, unless indicated otherwise in a credit line to the material. If material is not included in the article's Creative Commons licence and your intended use is not permitted by statutory regulation or exceeds the permitted use, you will need to obtain permission directly from the copyright holder. To view a copy of this licence, visit <http://creativecommons.org/licenses/by/4.0/>.

References

- H.U. Fuchs, *The dynamics of heat: A unified approach to thermodynamics and heat transfer*, 2nd edn. Graduate Texts in Physics (Springer Science+Business Media LLC, New York, 2010). <https://doi.org/10.1007/978-1-4419-7604-8>
- A. Feldhoff, *Energy Harvest. Syst.* **2**(1–2), 1 (2015). <https://doi.org/10.1515/ehs-2014-0040>
- A. Feldhoff, *Entropy* **22**(8), 1 (2020). <https://doi.org/10.3390/e22080803>
- C. Zener, *Trans. Am. Soc. Met.* **53**, 1052 (1961)
- A.F. Ioffe, *Semiconductor Thermoelements and Thermoelectric Cooling*, 1st edn. (Info-search Ltd., London, 1957)
- M. Wolf, R. Hinterding, A. Feldhoff, *Entropy* **21**(11), 1058 (2019). <https://doi.org/10.3390/e21111058>
- D. Narducci, *Appl. Phys. Lett.* **99**(10), 102104 (2011). <https://doi.org/10.1063/1.3634018>
- G. Tan, L.D. Zhao, M.G. Kanatzidis, *Chem. Rev.* **116**(19), 12123 (2016). <https://doi.org/10.1021/acs.chemrev.6b00255>
- J.Q. Guo, H.Y. Geng, T. Ochi, S. Suzuki, M. Kikuchi, Y. Yamaguchi, S. Ito, *J. Electron. Mater.* **41**(6), 1036 (2012). <https://doi.org/10.1007/s11664-012-1958-0>
- S.J. Poon, *Metals* **8**(12), 989 (2018). <https://doi.org/10.3390/met8120989>
- J. Shuai, J. Mao, S. Song, Q. Zhang, G. Chen, Z. Ren, *Mater. Today Phys.* **1**, 74 (2017). <https://doi.org/10.1016/j.mtphys.2017.06.003>
- Q. Zhang, Y. Sun, W. Xu, D. Zhu, *Adv. Mater.* **26**(40), 6829 (2014). <https://doi.org/10.1002/adma.201305371>
- J.W. Fergus, *J. Eur. Ceram. Soc.* **32**(3), 525 (2012). <https://doi.org/10.1016/j.jeurceramsoc.2011.10.007>
- O. Jankovsky, D. Sedmidubsky, Z. Sofer, P. Simek, J. Hejtmánek, *Ceramics-Silikáty* **56**(2), 139 (2012)
- Y. Miyazaki, M. Onoda, T. Oku, M. Kikuchi, Y. Ishii, Y. Ono, Y. Morii, T. Kajitani, *J. Phys. Soc. Jpn.* **71**(2), 491 (2002). <https://doi.org/10.1143/JPSJ.71.491>
- Y. Miyazaki, *Solid State Ionics* **172**(1–4), 463 (2004). <https://doi.org/10.1016/j.ssi.2004.01.046>
- C.H. Lim, W.S. Seo, S. Lee, Y.S. Lim, J.Y. Kim, H.H. Park, S.M. Choi, K.H. Lee, K. Park, *J. Korean Phys. Soc.* **66**(5), 794 (2015). <https://doi.org/10.3938/jkps.66.794>
- D. Kenfaui, M. Gomina, J.G. Noudem, D. Chateigner, *Materials* **11**(7), 1 (2018). <https://doi.org/10.3390/ma11071224>
- F. Li, T.R. Wei, F. Kang, J.F. Li, *J. Alloys Compd.* **614**, 394 (2014). <https://doi.org/10.1016/j.jallcom.2014.06.117>
- L.D. Zhao, J. He, D. Berardan, Y. Lin, J.F. Li, C.W. Nan, N. Dragoe, *Energy Environ. Sci.* **7**(9), 2900 (2014). <https://doi.org/10.1039/c4ee00997e>
- J. Sui, J. Li, J. He, Y.L. Pei, D. Berardan, H. Wu, N. Dragoe, W. Cai, L.D. Zhao, *Energy Environ. Sci.* **6**(10), 2916 (2013). <https://doi.org/10.1039/C3EE41859F>
- M.S. Dresselhaus, G. Chen, M.Y. Tang, R.G. Yang, H. Lee, D.Z. Wang, Z.F. Ren, J.P. Fleurial, P. Gogna, *Adv. Mater.* **19**(8), 1043 (2007). <https://doi.org/10.1002/adma.200600527>
- H. Ohta, S. Kim, Y. Mune, T. Mizoguchi, K. Nomura, S. Ohta, T. Nomura, Y. Nakanishi, Y. Ikuhara, M. Hirano, H. Hosono, K. Koumoto, *Nat. Mater.* **6**(2), 129 (2007). <https://doi.org/10.1038/nmat1821>
- Y. Liu, L.D. Zhao, Y. Zhu, Y. Liu, F. Li, M. Yu, D.B. Liu, W. Xu, Y.H. Lin, C.W. Nan, *Adv. Energy Mater.* **6**(9), 1502423 (2016). <https://doi.org/10.1002/aenm.201502423>
- M. Mikami, N. Ando, R. Funahashi, *J. Solid State Chem.* **178**(7), 2186 (2005). <https://doi.org/10.1016/j.jssc.2005.04.027>
- F. Kahraman, M.A. Madre, S. Rasekh, C. Salvador, P. Bosque, M.A. Torres, J.C. Diez, A. Sotelo, *J. Eur. Ceram. Soc.* **35**(14), 3835 (2015). <https://doi.org/10.1016/j.jeurceramsoc.2015.05.029>
- M. Wolf, K. Menekse, A. Mundstock, R. Hinterding, F. Nietschke, O. Oeckler, A. Feldhoff, *J. Electron. Mater.* **48**(11), 7551 (2019). <https://doi.org/10.1007/s11664-019-07555-2>
- C. Chen, T. Zhang, R. Donelson, D. Chu, R. Tian, T.T. Tan, S. Li, *Acta Mater.* **63**, 99 (2014). <https://doi.org/10.1016/j.actamat.2013.10.011>

29. M. Bittner, N. Kanas, R. Hinterding, F. Steinbach, D. Groeneveld, P. Wemhoff, K. Wiik, M.A. Einarsrud, A. Feldhoff, *J. Eur. Ceram. Soc.* **39**(4), 1237 (2019). <https://doi.org/10.1016/j.jeurceramsoc.2018.10.023>
30. R. Hinterding, Z. Zhao, M. Wolf, M. Jakob, O. Oeckler, A. Feldhoff, *Open Ceramics* **6**, 100103 (2021). <https://doi.org/10.1016/j.oceram.2021.100103>
31. R.K. Gupta, R. Sharma, A.K. Mahapatro, R.P. Tandon, *Physica B* **483**, 48 (2016). <https://doi.org/10.1016/j.physb.2015.12.028>
32. F. Delorme, P. Diaz-Chao, E. Guilmeau, F. Giovannelli, *Ceram. Int.* **41**(8), 10038 (2015). <https://doi.org/10.1016/j.ceramint.2015.04.091>
33. G. Constantinescu, S.M. Mikhalev, A.D. Lisenkov, D.V. Lopes, A.R. Sarabando, M.C. Ferro, T.F.d. Silva, S.A. Sergiienko, A.V. Kovalevsky, *Materials* **14**(4) (2021). <https://doi.org/10.3390/ma14040980>
34. Q. Zhang, X. Ai, L. Wang, Y. Chang, W. Luo, W. Jiang, L. Chen, *Adv. Funct. Mater.* **25**(6), 966 (2015). <https://doi.org/10.1002/adfm.201402663>
35. W. Liu, X. Yan, G. Chen, Z. Ren, *Nano Energy* **1**(1), 42 (2012). <https://doi.org/10.1016/j.nanoen.2011.10.001>
36. M. Samanta, S.N. Guin, K. Biswas, *Inorg. Chem. Front.* **4**(1), 84 (2017). <https://doi.org/10.1039/C6QI00435K>
37. T. Janssen, A. Janner, A. Looijenga-Vos, P.M. De Wolff, *International Tables for Crystallography: 9.8 Incommensurate and Commensurate Modulated Structures*, 3rd edn. (Kluwer Acad. Publ. Dordrecht, 2004)
38. T. Janssen, G. Chapuis, M. de Boissieu, *Aperiodic Crystals: From Modulated Phases to Quasicrystals*, *International Union of Crystallography monographs on crystallography*, vol. 20 (Oxford University Press, Oxford, 2007)
39. K.M. Nam, J.H. Shim, D.W. Han, H.S. Kwon, Y.M. Kang, Y. Li, H. Song, W.S. Seo, J.T. Park, *Chem. Mater.* **22**(15), 4446 (2010). <https://doi.org/10.1021/cm101138h>
40. F.C. Kong, Y.F. Li, C. Shang, Z.P. Liu, *J. Phys. Chem. C* **123**(28), 17539 (2019). <https://doi.org/10.1021/acs.jpcc.9b02842>
41. M. Chen, B. Hallstedt, L.J. Gauckler, *J. Phase Equilibria* **24**(3), 212 (2003). <https://doi.org/10.1361/105497103770330514>
42. K.T. Jacob, P. Gupta, *J. Solid State Chem.* **221**, 57 (2015). <https://doi.org/10.1016/j.jssc.2014.09.013>
43. T. Paulauskas, R.F. Klie, J. *Undergr. Res. Univ. Ill. Chicago* **5**(1), 1 (2017). <https://doi.org/10.5210/jur.v5i1.7511>
44. C. Ftikos, B. Steele, *J. Eur. Ceram. Soc.* **14**(6), 501 (1994). [https://doi.org/10.1016/0955-2219\(94\)90119-8](https://doi.org/10.1016/0955-2219(94)90119-8)
45. J.Y. Cho, O.J. Kwon, Y.K. Chung, J.S. Kim, W.S. Kim, K.J. Song, C. Park, *J. Electron. Mater.* **44**(10), 3621 (2015). <https://doi.org/10.1007/s11664-015-3924-0>
46. M. Liu, C. He, J. Wang, W.G. Wang, Z. Wang, *J. Alloys Compd.* **502**(2), 319 (2010). <https://doi.org/10.1016/j.jallcom.2009.12.134>
47. Y. Huang, B. Zhao, X. Hu, S. Lin, R. Ang, W. Song, Y. Sun, *Dalton Trans.* **41**(36), 11176 (2012). <https://doi.org/10.1039/c2dt31346d>
48. DFG SPP 2005: Priority Programm Opus Fluidum Futurum-Rheology of Reactive, Multiscale, Multiphase Construction Materials. www.spp2005.de

Publisher's Note Springer Nature remains neutral with regard to jurisdictional claims in published maps and institutional affiliations.